Rare-Earth Doped Configurational Entropy Stabilized High Entropy Spinel Oxide as an Efficient Anchoring/Catalyst Functional Interlayer for High-Performance Lithium-Sulfur Battery

Arindam Chatterjee,[a] Dipsikha Ganguly,[b] Ramaprabhu Sundara,*[b] and Subramshu S. Bhattacharya*[a]

Lithium-sulfur batteries (LSBs) are one of the most promising and potential modern-day energy storage devices due to the low-cost sulfur-based cathode and remarkably high energy density (~2600 Wh kg^{-1}). However, the detrimental shuttle effect of lithium polysulfide (LiPS) and the sluggish electrochemical redox kinetics of lithium sulfide (Li$_2$S) formation restrict its commercial viability. Herein, we design a novel transition metal-rare earth high entropy oxide (TM-RE HEO) Co$_{0.08}$Mn$_{0.08}$Ni$_{0.08}$Fe$_{1.96}$Mg$_{0.08}$Nd$_{0.01}$Gd$_{0.01}$Sm$_{0.01}$Pr$_{0.01}$O$_4$ as a polysulfide adsorbent and catalyst for the redox reactions of sulfur species in Li–S battery. TM-RE HEO interlayer exhibits an excellent discharge capacity of 1146 mAh g^{-1} at 0.1 C rate, high rate capability, and reasonable long-term cycling stability at 0.5 C rate with a low capacity decay of 0.08% per cycle after 300 cycles. High degree of chemical confinement of soluble polysulfides, as demonstrated by the strong bonding between TM-RE HEO and Li$_2$S$_6$, and expedited catalytic conversion to insoluble Li$_2$S, result from strong polar catalytically active multiple metal sites and abundant oxygen vacancies. This work demonstrates the potential of high entropy oxide in developing high-efficiency LSB technology.

Introduction

Rational design and fabrication of electrochemical energy storage technology to meet the ever-increasing demand of electric vehicles and electronic devices are now top priority. Considerable focus on research in lithium-sulfur batteries (LSBs) has been put in the past few years. High theoretical specific capacity of 1675 mAh g^{-1} and high energy density of 2600 Wh g^{-1} as well as low cost, non-toxic, earth-abundant sulfur sources draw considerable attention to LSBs as energy storage devices.[1,2] The sulfur cathode undergoes a complex conversion process from solid cyclic-S$_8$ molecules to a series of soluble lithium polysulfides (LiPS) intermediates (Li$_2$S$_8$, Li$_2$S$_6$, Li$_2$S$_4$; 2.4–2.2 V vs. Li/Li$^+$) and fully to Li$_2$S$_2$/Li$_2$S (2.2–1.8 V vs. Li/Li$^+$).[3,4] The notorious shuttle effect originating from soluble LiPS is a major drawback in achieving long cycling stability in LSBs.[5,6] Significant efforts have been made to address the

shuttling issue by confining S in a host material, entrapping soluble LiPS for improving rate capability, but have so far been unable to completely eliminate the dissolution of LiPS into the electrolyte.[7–10] Porous carbons matrices such as carbon nanotubes, mesoporous carbon were considered as good options to encapsulate sulfur in the porosity sites owing to their superior electron pathways and 3D interconnected nature,[11–13] partially confining polysulfides by physical interaction with LiPSs.[14] However, the conjugate non-polar carbon planes have limited active sites to strongly anchor polar LiPSs. Electrochemical active transition metal oxides were reported as electrocatalysts to accelerate the conversion of soluble LiPS to final product Li$_2$S[15,16] and are also emerging as polar host materials to LiPS. Polar electrocatalyst can greatly enhance the electrochemical kinetics of sulfur redox reactions and suppress the shuttle effect by chemical confinement of sulfur species, and effectively improve the cycling stability of sulfur cathode.[17–20] Compared with carbon materials, metal oxides afford abundant efficient anchoring polar active sites, which is beneficial for adsorption of polysulfides as well as suppression of the shuttle effect of polysulfides.[21] Exploring and developing new materials for achieving adsorption catalysis on the conversion of soluble LiPS is the need of the hour. Catalytic activity is strongly related to metal cations vacancy, and recently, multicomponent metal oxides are being fervently explored as the material for regulating soluble LiPS due to its abundant vacancies and tunable exposed surface.[22,23] Liang et al. prepared TiO$_2$ nanowires-supported CNT via hydrothermal method, utilized as polysulfide barrier to suppress the shuttle effect.[24] Zhang et al. showed bifunctional Ba$_{0.5}$Sr$_{0.5}$Co$_{0.8}$Fe$_{0.2}$O$_{3-\delta}$ perovskite as catalyst

[a] A. Chatterjee, Prof. S. S. Bhattacharya
Department of Metallurgical and Materials Engineering
Nano Functional Materials Technology Centre (NFMTC)
Indian Institute of Technology Madras
Chennai, 600036 (India)
E-mail: ssb@iitm.ac.in

[b] D. Ganguly, Prof. R. Sundara
Department of Physics
Alternative Energy and Nanotechnology Laboratory (AENL)
Nano Functional Materials Technology Centre (NFMTC)
Indian Institute of Technology Madras
Chennai, 600036 (India)
E-mail: ramp@iitm.ac.in

📖 Supporting information for this article is available on the WWW under https://doi.org/10.1002/batt.202300082

for LiPS conversion and Li_2S deposition.[25] Liang et al.[26] proposed δ-MnO_2 nanosheets for chemically binding polysulfides strongly, since the existence of thiosulfate and the reduction of Mn ions in δ-MnO_2 confirm the redox reaction between polysulfide and δ-MnO_2.[26] Wang et al. demonstrated CNT/$NiFe_2O_4$-S ternary hybrid material consisting of highly conductive CNTs as electron conduction framework and non-conductive polar spinel oxide $NiFe_2O_4$ as strong polysulfide adsorber since the conductivity of the material determines the kinetics of electron transfer which significantly effects the conversion of sulfur to Li_2S.[27] High entropy oxides (HEOs) consisting of five or more principal elements randomly distributed in a single phase crystal structure also hold great potential due to presence of polar surface for high adsorption of reaction intermediates.[28,29] Qiao et al. synthesized a rock-salt type (NiMgCoCuZn)O and proved that regular nanostructure is essential for highly efficient catalyst in LSBs.[30] Gao et al. synthesized ($Zn_{0.2}Co_{0.2}Mn_{0.2}Ni_{0.2}Mg_{0.2}$)$Fe_2O_4$ HEO nanofibers via electrospinning method, and used them as a sulfur host to catalyze the conversion of LiPSs.[31] Qiao et al.[30] prepared (ZnCuNiMgCoNi)O HEO which mediated the immobilization of LiPS in sulfur cathode. Randomized structure is highly conducive to exposure of affluent active sites to confine LiPSs. Rare earth elements, being more electronegative, have strong adsorbent property towards Lewis basic polysulfides. They can also serve as an electrocatalyst by reducing energy barrier for Li_2S nucleation.[32] Transition metals can effectively lower activation energy barrier of Li_2S, leading to low polarization and consequently, an excellent rate performance. They also decrease the surface work function which in turn increases charge transfer ability, leading to improved catalytic oxidation of Li_2S.[33]

In this study, we design and synthesize a novel transition metal-rare earth high entropy oxide (TM-RE HEO) spinel of irregularly shaped nanoparticles via a facile reverse co-precipitation (RCP) method for use as an interlayer to anchor the polysulfides as well as to facilitate the conversion of soluble LiPS and control the kinetics of electrochemical reactions at the sulfur cathode in LSBs. Strong polar active sites of transition metals anchor the LiPSs. This behavior can be further improved by substituting with the more electronegative rare-earth elements. Synergistic functions of all electrochemically active metal cations in TM-RE HEO catalyze the conversion of reaction intermediates. Hence, excellent cycling stability can be observed for the TM-RE HEO interlayer, meeting the demand for LSB rate performance. For the first time, a novel high entropy oxide involving multiple transition metals and rare-earth cations has been designed and developed as a potential material for improved LSB performance.

Results and Discussion

X-ray diffraction (XRD) patterns of TM-RE HEO clearly demonstrate that all predominant diffraction peaks are well indexed to the cubic (Fd-3 m) spinel crystal structure (JCPDS 89-4927) and XRD results also reveals that TM-HEO adopts a cubic crystal

phase with space group of Fd-3 m, as given in Figure 1(a). Schematic illustration of the crystal structure of TM-RE HEO is presented in Figure 1(b). The crystallite size determined by the Scherrer formula from XRD pattern (Figure 1a) is 39 nm. Scanning electron microscopy (SEM) reveals the irregular shape morphology of the TM-RE HEO nanoparticles prepared via RCP process having diameter of 500 ± 116.3 nm, see Figure 1(c). SEM micrographs of TM-HEO exhibits semi-spherical shape particles, while TM-REO CNT forms well-expected nanotubes, see Figure 1(d and e). Energy dispersive spectroscopy (EDS) result demonstrates that the atomic concentrations of the elements are well in agreement with the expected stoichiometry (Tables S1–S3, Supporting Information). Transmission electron microscopy (TEM) analysis was conducted to further investigate the microstructural details of the material. The morphology of TM-RE HEO can be ascribed as irregular-shaped from the TEM micrograph and polycrystalline particles confirmed by the SAED ring pattern. High-Resolution HRTEM image shows well-defined lattice fringe d-spacing of 0.17 nm corresponding to (224) reflection plane of cubic spinel structure, indicating high crystallinity of the material, as shown in Figures 1(f and g). All the diffraction rings in selected area electron diffraction (SAED) pattern in Figure 1(h), are well-consistent with the XRD measurements, suggesting that the as-prepared TM-RE HEO belongs to the cubic crystal structure with *Fd-3 m* space group. Elemental-mapping results demonstrate that all elements are homogeneously distributed throughout the particles without significant accumulation or segregation of individual elements, confirming highest possible configurational entropy, as depicted in Figure 1(i). XPS study was performed to examine the surface oxidation states of the TM-RE HEO material. Determining oxidation states of a randomized homogeneously distributed structure of transition and rare-earth elements with high precision and without an exact reference is nearly impossible because the ionization energy can shift due to varying local elemental environment. XPS spectra reveal signatures from ten main elements: cobalt (Co 2p), manganese (Mn 2p), magnesium (Mg 2p), nickel (Ni 2p), iron (Fe 2p), neodymium (Nd 3d), samarium (Sm 3d), praseodymium (Pr 3d), gadolinium (Gd 4d) and oxygen (O 1s), as depicted in Figure 2(a–j). Inductively coupled plasma optical emission spectrometer (ICP-OES) is employed to determine the concentrations of the constituent elements (Table S4a and b, Supporting Information) and to calculate the configurational entropies of TM-RE HEO and also TM-HEO based on Boltzmann-Gibbs interpretation,[22] that turns out to be more than 1.5R and consequently, are defined as high entropy materials. Further, the electron paramagnetic resonance (EPR) spectrum recorded for the TM-RE HEO shows large asymmetry, indicating the presence of oxygen vacancies as also observed in the EPR spectrum of TM-HEO, displayed in Figure 2(k).

The high-resolution XPS (HR-XPS) spectrum pertaining to each element was used to determine their oxidation states as well as get an idea of the oxygen vacancies. The co-2p spectrum shows two major peaks at 780.6 and 791.6 eV corresponding to Co $2p_{3/2}$ (Co^{3+}) and Co$2p_{1/2}$ (Co^{3+}) ionizing energies respectively, with an additional satellite peak at
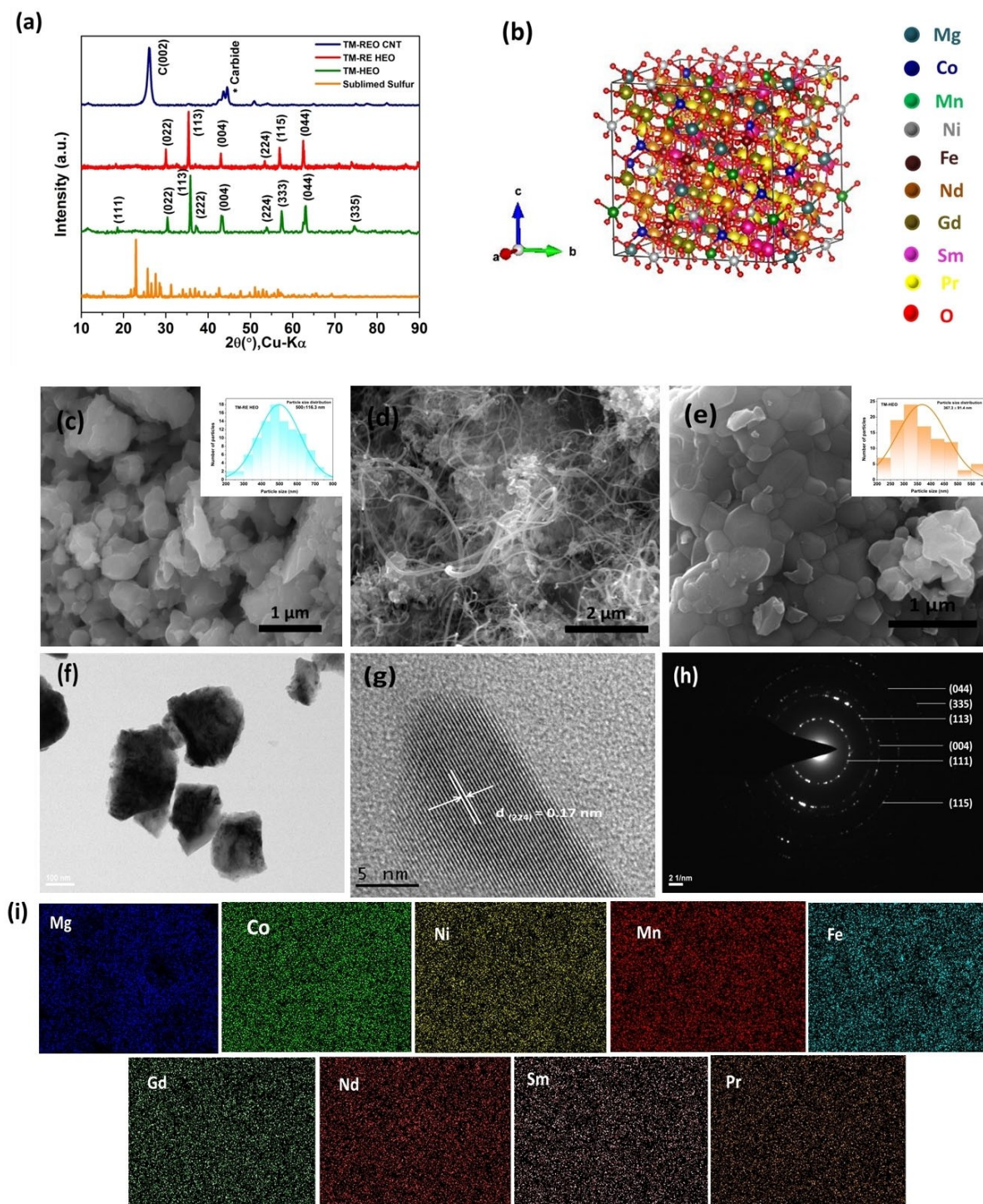
Figure 1. Structural and morphological characterization of TM-RE HEO, TM- HEO, TM-REO CNT. a) XRD patterns; b) schematic illustration of crystal structure of TM-RE HEO drawn in Vesta; c–e) SEM images of TM-RE HEO, TM-REO CNT and TM-HEO (inset figure is particle size distribution); f) TEM image; g) high-resolution TEM (HRTEM) image; h) SAED pattern of TM-RE HEO; i) elemental mapping of the as-synthesized TM-RE HEO.

785.5 eV.[34] The peak at 641.6 eV of the Mn $2p_{3/2}$ spectrum confirms the presence of Mn^{2+} (Mn $2p_{3/2}$). The peak located at 646.4 eV is a satellite peak of Mn $2p_{3/2}$. The peak at 653.0 eV belongs to Mn^{3+} (Mn $2p_{1/2}$).[34] The high-resolution XPS Ni 2p spectrum shows two spin-orbit peaks at 855.2 and 872.8 eV, which can be ascribed to Ni $2p_{3/2}$ and Ni $2p_{1/2}$ respectively. One

shake-up satellite peak Ni $2p_{1/2}$ was detected at the high binding energy side around 861.4 eV, and another one is seen at the low ionization energy side at 848.7 eV. Peak at around 879.7 eV corresponds to Ni^{3+} (Ni $2p_{1/2}$).[34] Fe 2p spectrum shows peaks at around 710.6 and 724.8 eV, which are attributed to spin-orbit peaks at Fe $2p_{3/2}$ (Fe^{2+}) and Fe $2p_{1/2}$ (Fe^{3+})
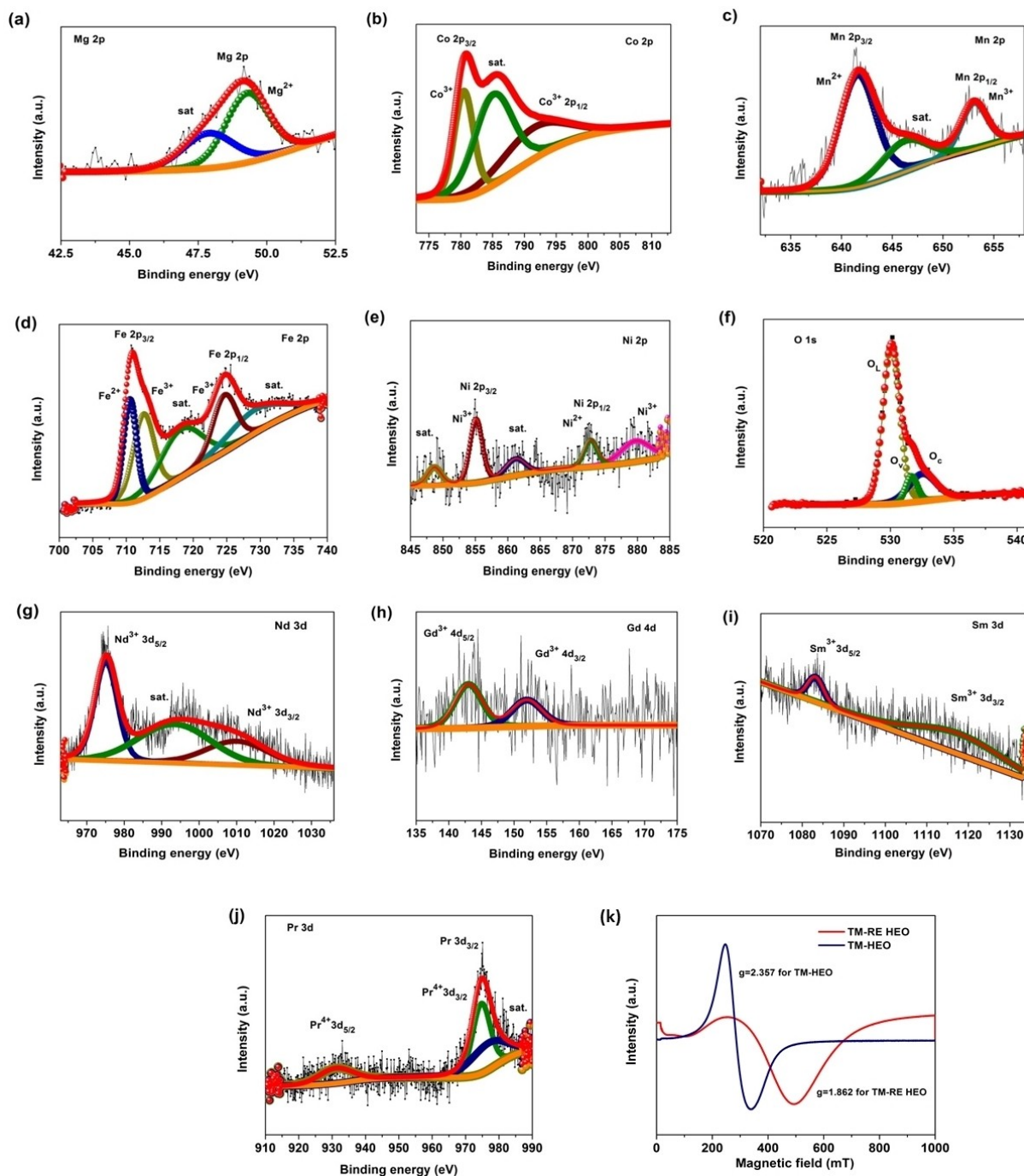
Figure 2. XPS spectra of TM-RE HEO, a) Mg 2p, b) Co 2p, c) Mn 2p, d) Fe 2p, e) Ni 2p, f) O 1s, g) Nd 3d, h) Gd 4d, i) Sm 3d, j) Pr 3d, k) EPR spectra of TM-RE HEO and TM-HEO.

respectively. Two satellite peaks belonging to Fe $2p_{3/2}$ and Fe $2p_{1/2}$ are located at 718.3 and 729.4 eV respectively. The peak at a binding energy of 712.7 eV (Fe $2p_{3/2}$) is attributed to the presence of Fe^{3+}.[34] The O-1 s spectra can be de-convoluted into three major peaks situated at 530.0,531.6 and 532.6 eV, which are attributed to lattice oxygen O_L, oxygen vacancies O_V and chemisorbed oxygen O_C respectively.[34] The Mg 2p spectrum is de-convoluted into a peak at 49.2 eV which belongs to Mg^{2+} and a satellite peak at 48.0 eV attributed to

Mg^{2+} in a different environment.[35] The Nd 3d spectrum shows spin-orbit peaks located at 975 eV which belongs to Nd $3d_{5/2}$ (Nd^{3+}), while the peak at 1011.5 eV corresponds to Nd $3d_{3/2}$ (Nd^{3+}).[36] One satellite peak (Nd^{3+}) is found at 994.5 eV.[37] In the Gd 4d spectrum, the spin-orbit peak located at 143.2 eV can be ascribed to Gd $4d_{5/2}$(Gd^{3+}) and the peak at 151.8 eV is assigned to Gd $4d_{3/2}$ (Gd^{3+}).[38] In Sm 3d spectrum, two peaks situated at 1083.5 and 1117.4 eV which can be assigned to two spin-orbit peaks of Sm $3d_{5/2}$ (Sm^{3+}) and Sm $3d_{3/2}$ (Sm^{3+})

Batteries & Supercaps

Research Article
doi.org/10.1002/batt.202300082

Chemistry
Europe

European Chemical
Societies Publishing

respectively.[39] In Pr 3d spectrum, two peaks at 931.6 and 974.5 eV can be ascribed to Pr $3d_{5/2}(Pr^{4+})$ and Pr $3d_{3/2}(Pr^{4+})$ respectively. One satellite peak due to Pr $3d_{3/2}$ is seen at 981.4 eV.[40,41]

To validate the influence of TM-RE HEO in polysulfide entrapment in LSBs, the electrochemical properties of TM-RE HEO are evaluated. Cyclic voltammetry (CV) curves of three samples are presented in Figure 3(a). All the samples exhibit two cathodic peaks (C_2, C_1) located at 2.2–2.4 V vs. Li/Li$^+$ and 1.9–2.1 V vs. Li/Li$^+$ respectively, which can be attributed to the

formation of long-chain polysulfides and further conversion to insoluble Li$_2$S respectively.[42] Anodic peak (A) situated at 2.3–2.5 V vs. Li/Li$^+$ corresponds to the reversible oxidation process of solid Li$_2$S. The sharp cathodic peak of TM-RE HEO is due to the conversion of LiPSs.[43–45] Galvanostatic charge-discharge test were performed in the potential window of 1.8–2.8 V at different C rates. Charge-discharge profiles of TM-RE HEO, TM-HEO, and TM-REO CNT at the initial cycle are shown in Figure 3(b). The two sharp cathodic peaks (C_2, C_1) of TM-RE HEO, TM-HEO, TM-REO CNT in Figure 3(a) are well-consistent
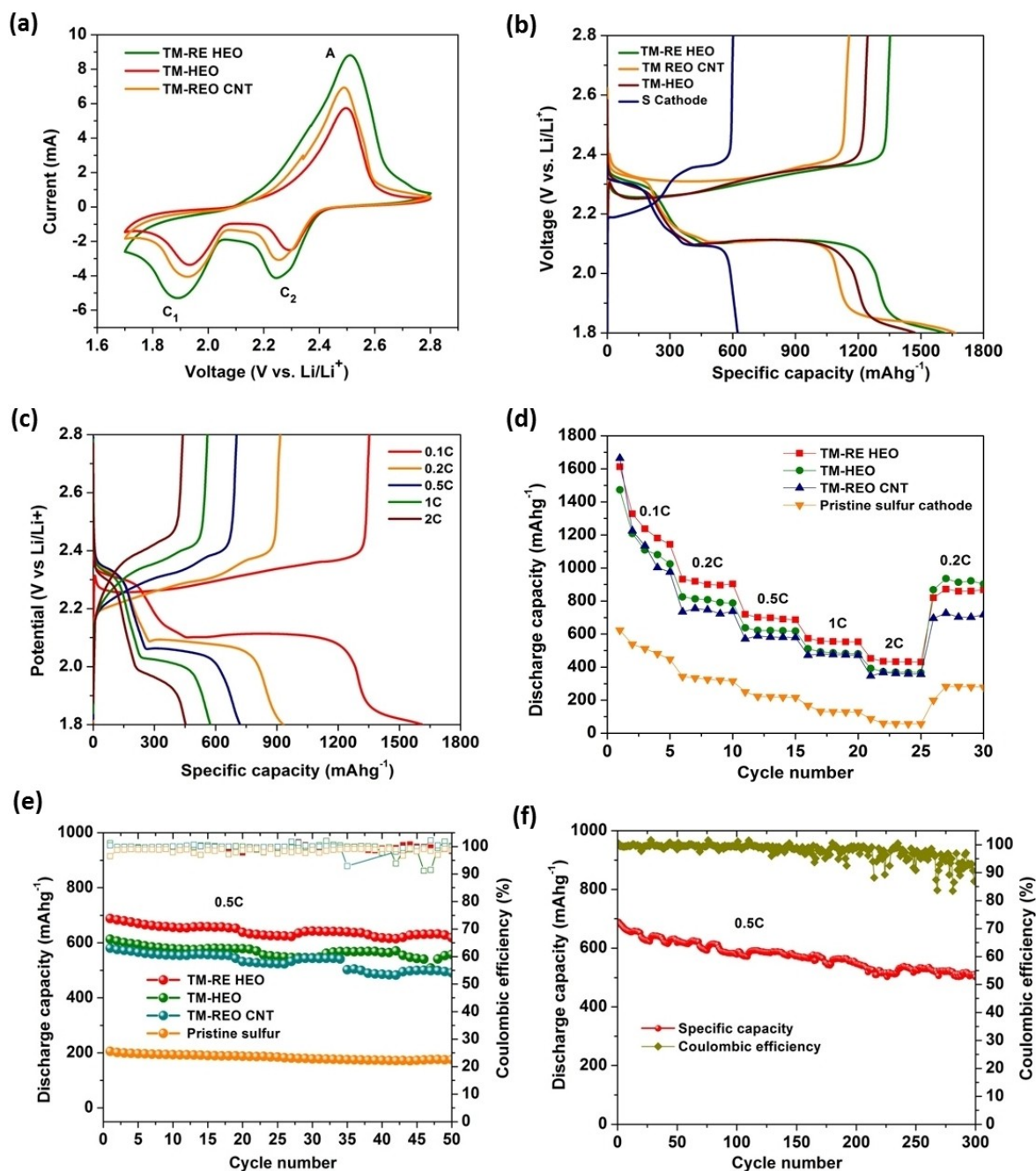

Figure 3. Electrochemical properties evaluation. a) CV curves of TM-RE HEO, TM-HEO and TM-REO CNT. b) Initial galvanostatic discharge-charge curves of TM-RE HEO, TM-REO CNT, TM-HEO, S cathode in the voltage range of 1.8 to 2.8 V at 0.1 C rate, c) Charge-discharge profiles of TM-RE HEO at different C rates, d) rate capability, e) rate-performance test at 0.5 C rate of four samples, f) cyclic performance of TM-RE HEO after 300 cycles at 0.5 C rate.

with the two plateaus in the discharge curves of Figure 3(b). The anodic peak (A) is also in-line with the one plateau in charge curves of Figure 3(b). TM-RE HEO delivers discharge specific capacities of 1148, 910, 690, 556, and 432 mAh g^{-1} at the rates of 0.1 C, 0.2 C, 0.5 C, 1 C, and 2 C with 5 cycles at each rate, see Figure 3(c). Further, at 0.2 C after cycling at various C rates, a reversible capacity of 868 mAh g^{-1} is obtained, demonstrating excellent rate capability of TM-RE HEO material (Figure 3d). TM-RE HEO interlayer exhibits a discharge specific capacity of 580 mAh g^{-1} at 0.5 C after 300 cycles which is 84% of the initial capacity. In contrast, the pristine S cathode without any functional interlayer delivers a discharge capacity of only 156 mAh g^{-1} after 50 cycles, indicating significant capacity decay compared to TM-RE HEO interlayer. The discharge capacity of TM-RE HEO exhibits 511 mAh g^{-1} after 300 cycles with a very low capacity fading rate of 0.08% per cycle as well as a high Coulombic efficiency of 93.1%. It suggests that the shuttle effect of polysulfides is greatly restricted by the strong entrapment of sulfur species in TM-RE HEO and better redox kinetics. In contrast, TM-REO CNT suffers from lower specific capacity and rapid capacity fading due to weak adsorption of polysulfides, as shown in Figures 3(e and f). SEM was performed after 100 cycles to examine the morphological evolution of TM-RE HEO, TM-HEO, and TM-REO CNT interlayer. Better cycling stability and excellent rate capability of TM-RE HEO compared to TM-HEO, TM-REO CNT, and pristine sulfur cathode demonstrate its potential to be used in polysulfide entrapment.

Redox kinetics of sulfur cathodes are explored from the CV curves of TM-RE HEO, TM-HEO, and TM-REO CNT at various scan rates (0.1, 0.2, 0.4, 0.6, and 0.8 mV s^{-1}) with the corresponding peak current versus square root of scan rate of all materials plotted linearly, as presented in Figure 4(a and b). The linear fitted slope reflects the diffusion kinetics of Li-ion in the electrode according to Randles-Sevcik equation.[46] TM-RE HEO shows higher slopes at both cathodic and anodic peaks, elucidating faster Li-ion diffusion in redox reactions. Diffusion coefficient of Li$^+$ ion D_{Li^+} corresponding to the cathodic peak (C$_1$) current of TM-RE HEO interlayer is 2.783×10^{-10} cm^{2}s^{-1}, while for another cathodic peak (C$_2$) current is 2.343×10^{-10} cm^{2}s^{-1}, and for anodic peak (A) current is 7.1135×10^{-10} cm^{2}s^{-1}. TM-HEO interlayer has diffusion coefficient of 8.65×10^{-11} cm^{-2}s^{-1} corresponding to cathodic peak (C$_1$) and 6.778×10^{-11} cm^{2}s^{-1} corresponding to the other cathodic peak (C$_2$) and D_{Li^+} at anodic peak is 2.283×10^{-10} cm^{2}s^{-1}. TM-REO CNT has diffusion coefficient of 1.723×10^{-10} cm^{2}s^{-1} at cathodic peak current (C$_1$). Linear dependency reflects smooth step-wise Li$^+$ diffusion processes. The redox peaks maintain stable form except for a minor peak shift, and slight peak separation even at higher scan rates, demonstrating good electrochemical durability and strong catalytic ability for the conversion of LiPSs (Figure 4c). Faster Li$^+$ diffusion of TM-RE HEO is more conducive to facilitate redox reaction kinetics. Reduction peaks shift to positive potential while the oxidation peak shifts to negative potential in TM-RE HEO compared to rare-earth undoped TM-HEO and higher peak current intensity of TM-RE HEO elucidates lower electrochemical polarization and accel-

erates the redox kinetics of sulfur species. In addition, the overlapping of CV curves of TM-RE HEO for five cycles indicates its excellent cycling reversibility resulting from the strong adsorption effect and catalytic activity of the polar TM-RE HEO material. Sulfur cathode involves transformation from solid S$_8$ molecules to soluble long-chain LiPS and then solid-state Li$_2$S$_2$/Li$_2$S. TM-RE HEO interlayer shows higher peak current and lower charge transfer resistance, suggesting faster reaction kinetics on the conversion of LiPS to Li$_2$S. The Tafel slopes derived from CV curves are shown in Figure 4(d). TM-RE HEO exhibits a Tafel slope of 122.9 mV dec^{-1} which is lower compared to TM-HEO (133.4 mV dec^{-1}) and TM-REO CNT (173.8 mV dec^{-1}), indicating relatively lower activation energy barrier of TM-RE HEO to the conversion from Li$_4$S$_2$ to Li$_2$S which is the rate-determining step of the redox process. Nyquist plot after 5th cycle of each of the four samples are shown in Figures 4(e and f). The dissolution of LiPS into electrolyte increases the electrolyte resistance (R_e).[47] Subsequent decline in discharge is caused due to reduction of soluble LiPS to Li$_2$S$_2$/Li$_2$S and strong chemical entrapment of LiPS in the TM-REO HEO interlayer. Low adsorption and diffusion impedance is attributed to fast kinetics of LiPS conversion on TM-REO HEO layer. The mid-frequency semicircle and low-frequency sloping line could be due to the deposition of Li$_2$S on the electrode surface.[48]

Chemical adsorption of polysulfide species could alleviate the shuttling effect of LiPS. To further understand the adsorption-catalysis performance, the intuitive adsorption study of soluble LiPS on HEO was performed. A chemical adsorption study was executed by using 2 mM Li$_2$S$_6$ solution to examine the binding effect between HEO and LiPS. The yellow-colored Li$_2$S$_6$ solution containing TM-RE HEO faded in 8 h and is observed from the lowering of the intensity of the absorption peak of Li$_2$S$_6$ in the visible light range after adding TM-RE HEO, whereas solutions containing TM-HEO and TM-REO CNT take longer times to become colorless, elucidating comparatively stronger adsorption of Li$_2$S$_6$ molecules to TM-RE HEO (see Figure 5a). It demonstrates that chemical interaction is an influential factor for the efficient anchoring ability of LiPS, instead of surface area as physical adsorption.[49] UV-visible absorption spectrum shows weaker absorption peaks of TM-RE HEO, demonstrating that TM-RE HEO can strongly trap soluble LiPS. Innovative research for advanced interlayer systems will play an essential role in the practical advancements of LSBs.

Fourier Transform Infrared (FT-IR) spectra (Figure 5b) of TM-RE HEO, TM-HEO reveals some characteristic IR bands belonging to the polysulfide structure, which demonstrates the strong adsorption property of the high entropy metal oxides. FT-IR spectra of TM-RE HEO show a peak at 1054 cm^{-1} which can be ascribed to the S—O symmetric vibration, while the peak around 1130 cm^{-1} is assigned to S=O antisymmetric vibrations. S=O symmetric vibration peak located at 1343 cm^{-1}. S—O antisymmetric vibration peak is found around 1607 cm^{-1}.[50]

Post-mortem analysis of the cycled interlayer is crucial in exploring the morphological evolution that reveals the capacity attenuation. TM-REO CNT and TM-HEO interlayers were disassembled after 120 cycles at 0.5 C, to investigate the microstructural changes by SEM and EDS elemental mapping, as
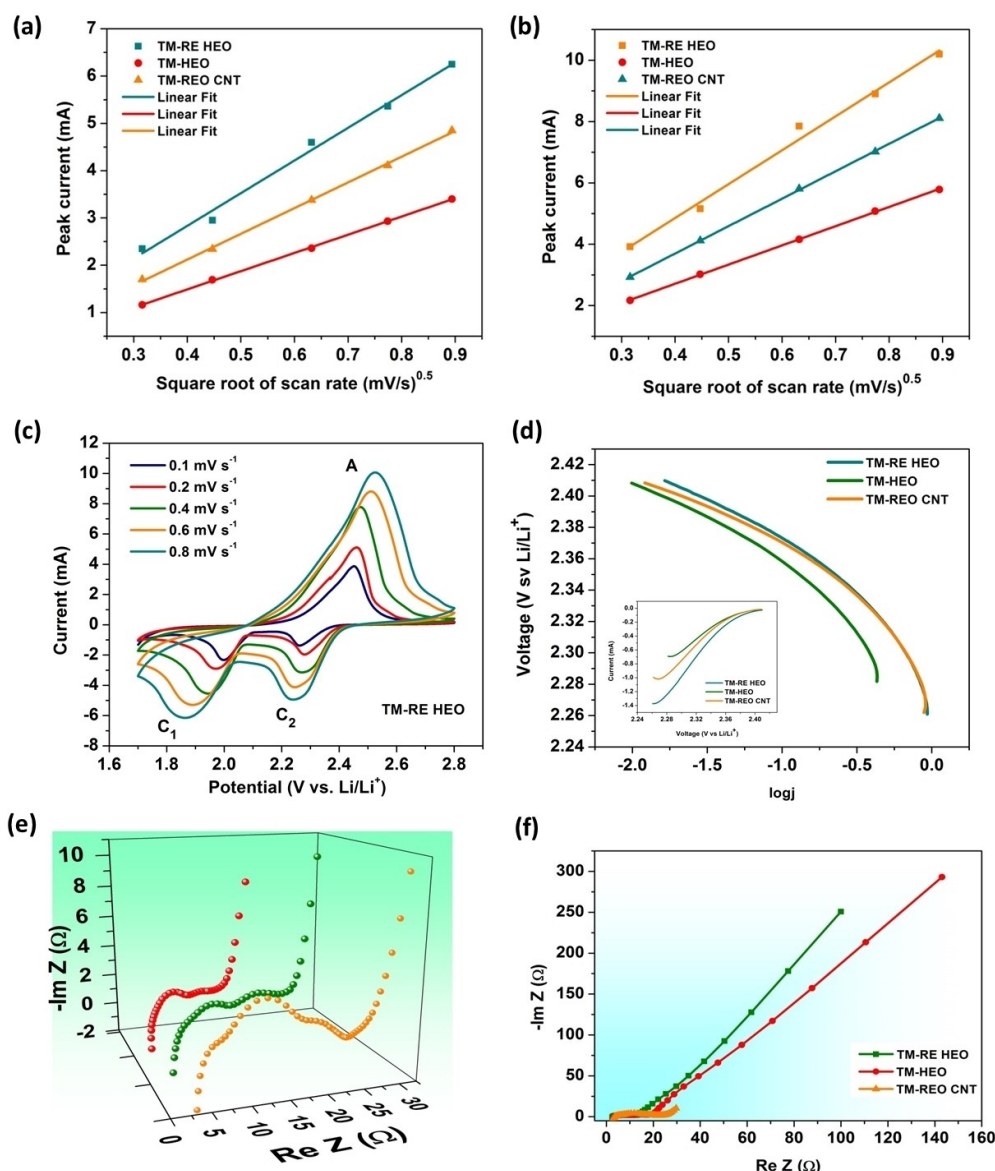
Figure 4. Diffusion co-efficient of TM-RE HEO, TM-HEO and TM-REO/CNT at a) C_1 peak and b) O peak, c) CV curves of TM-RE HEO at various scan rates, d) Tafel plots of TM-RE HEO, TM-HEO and TM-REO/CNT, e and f) Nyquist plots of 3 samples.

shown in Figures 6(a and b). TM-HEO morphology reveals the formation of dendrites, and non-uniform Li-deposition. TM-REO CNT surface morphology demonstrates no obvious crack formation, so morphology is well-maintained. The post-mortem SEM image of TM-RE HEO (Figure 6c) interlayer after 300 cycles at 0.5 C reveals no particle fragmentation, suggesting the morphology remains intact; elemental mapping shows uniform distribution of elements that indicates configurational entropy stabilization of high entropy materials.

XPS analysis of TM-RE HEO before and after adsorption of Li_2S_6 was conducted to validate the adsorption of polysulfides to the polar active sites and synergistic effects of constituent elements towards the improvement of conversion kinetics of soluble LiPSs. The interaction of TM-RE HEO with Li_2S_6 is essentially observed from the O1s spectra. Figure 7(a) shows that O1s spectra of TM-RE HEO exhibits peaks located at 530.1,

531.6 and 532.6 eV, which can be ascribed to lattice oxygen (O^{2-}), oxygen vacancies and chemisorbed oxygen respectively.[51] The peak corresponding to lattice oxygen shifted by 1.8 eV to higher binding energy values upon exposure to the Li_2S_6, which is attributed to the interaction between Li and O.[52,53] Earlier reports suggested that the catalytic activity could be enhanced with the increase in the binding energy of O1s spectra,[54] which in turn enables O species of TM-RE HEO to form bonds with Li of LiPSs. Moreover, the intensity of the lattice oxygen peak reduced after adsorption of Li_2S_6, manifesting the increasing affinity of TM-RE HEO to Li_2S_6.

Figure 7(b) presents the XPS survey scan of TM-RE HEO before and after the adsorption of Li_2S_6. The survey scan revealed that the peak of Nd 3d spectrum at 975 eV, Gd 4d spectrum at 151.8 eV, Pr 3d spectrum at 931.6 eV, Ni 2p
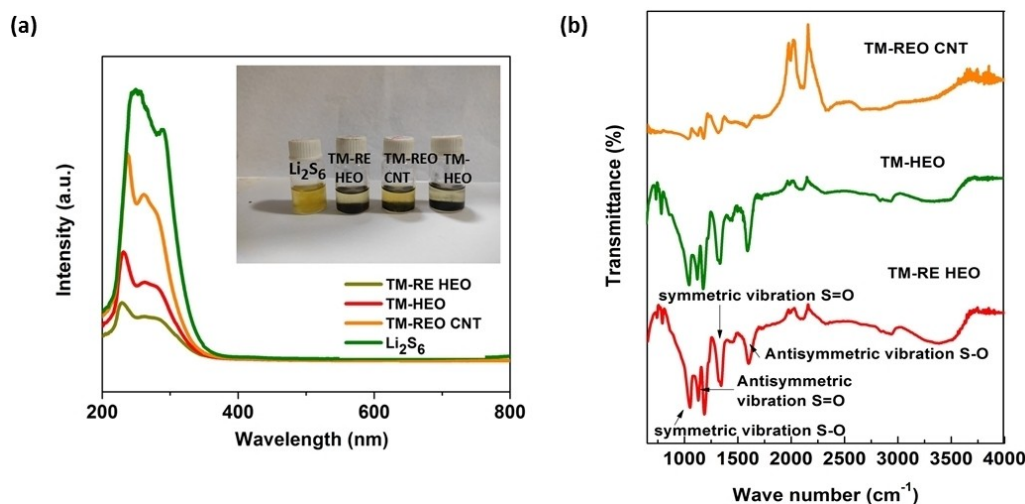
Figure 5. a) Adsorption study of LiPS on TM-RE HEO, TM-HEO, TM-REO CNT: UV-vis spectra of the Li_2S_6 solution after complete adsorption of different polysulfides. Inset shows the photograph of the optical absorption test. b) FT-IR spectra of TM-RE HEO, TM-HEO, TM-REO CNT.
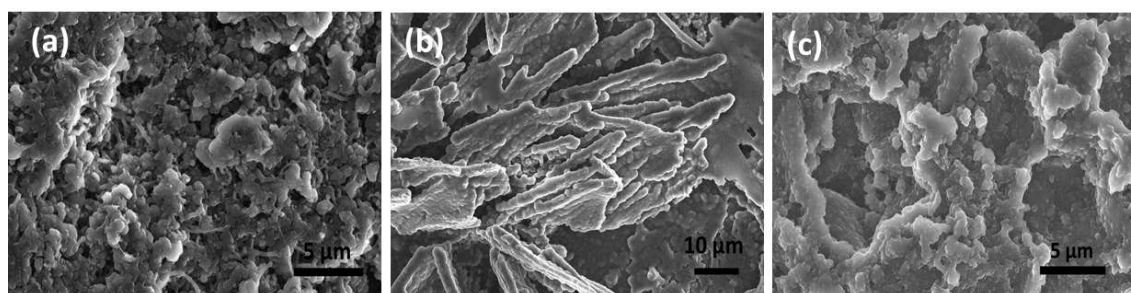

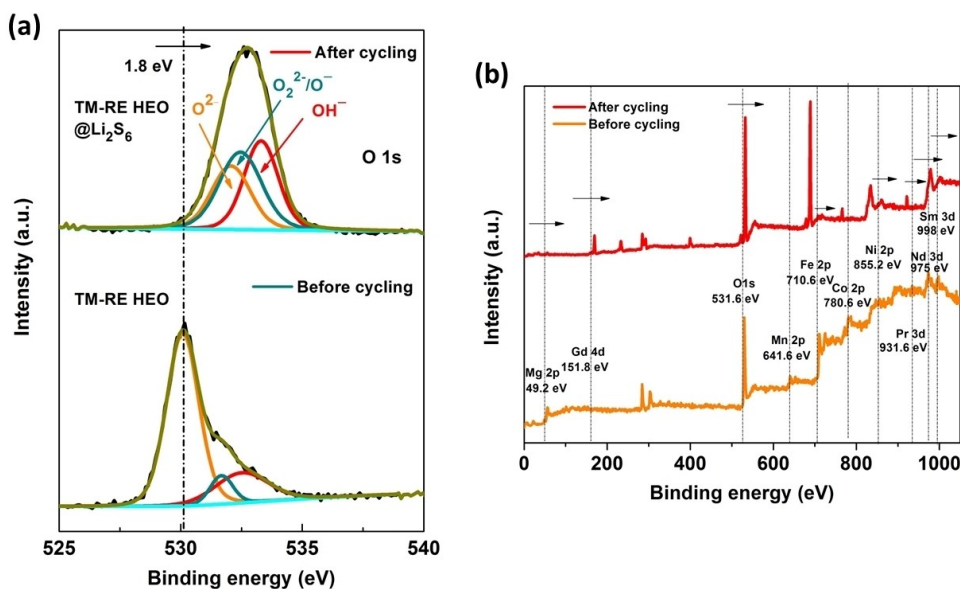**Figure 6.** Post-mortem SEM analysis of a) TM-REO CNT, b) TM-HEO and c) TM-RE HEO.

Figure 7. a) High resolution XPS spectra of O1s; b) XPS survey spectra of TM-RE HEO.

spectrum at 855.2 eV, Fe 2p spectrum at 710.6 eV and, Mg 2p spectrum at 49.2 eV all had shifted to higher binding energy values after adsorption of Li_2S_6. This is a clear indication that

the TM-RE HEO has an increased chemical affinity to the LiPSs due to the strong redox capability of both rare-earth and transition metal species.[55] These all important binding energy

Batteries & Supercaps

Research Article
doi.org/10.1002/batt.202300082

Chemistry Europe
European Chemical
Societies Publishing

shifting reflects the chemical anchor effect and transfer of electrons between TM-RE HEO and Li_2S_6, which is favorable for enhancing electrochemical performance. Briefly, XPS analysis reveals the chemical interaction between TM-RE HEO and LiPSs, suggesting 1) Li–O and metal-sulfur bondings effectively immobilize the LiPSs; 2) the synergistic effect of multiple metal elements in TM-RE HEO contributes to the polysulfide entrapment and electrochemical conversion.[56,57]

The oxygen vacancies can also effectively increase the binding energy between TM-RE HEO and lithium polysulfides (LiPSs) as well as, reduce the energy barrier of the LiPSs decomposition reaction,[58] which in turn, promotes/accelerates the LiPSs conversion reaction kinetics.[59,60] Adsorption experiments and, ex situ XPS results prove that the oxygen vacancies improve the adsorption performance of TM-RE HEO to LiPSs and can effectively inhibit the shuttle effect of LiPSs.

Nazar et al.[61] had reported that single metal oxide MnO_2 nanosheets as a functional interlayer exhibited capacity retention of only 93% after 100 cycles at a low 0.2 C rate with an even lower sulfur loading of 0.7 mg cm^{-2} while Gope and Bhattacharyya[62] employed NiO as an interlayer which showed stable cycling stability only up to 100 cycles. Likewise, Kang et al.[63] reported on an MgO interlayer in carbon matrix which exhibited capacity retention of only 78.3% after 200 cycles at 0.2 C rate. On the other hand, the TM-RE HEO interlayer in the present study exhibits long-term cycling stability at 0.5 C rate with as low a capacity decay of 0.08% per cycle after 300 cycles at a comparatively higher sulfur loading of 1.5 mg cm^{-2}. Therefore, it is clear that the use of TM-RE HEO as a functional interlayer contributes both to the polysulfide entrapment and improved electrochemical conversion owing to the synergistic effect of the multiple metallic and rare earth elements[30] in the high entropy form.

Configurational entropy stabilized TM-RE HEO, TM-HEO comprising high catalytic active sites on polar surfaces greatly enhances the sulfur redox reactions. Also, TM-REO CNT is further studied for the fundamental understanding of the effect of CNT on cycling stability and comparison with the performance of high entropy oxides as interlayer in LSBs. The specific capacity and rate capability comparison amongst TM-HEO, TM-RE HEO, TM-REO CNT, and sulfur indicates that multicomponent high entropy oxides are more suitable in preventing polysulfide from dissolution owing to synergistic effects of different elements, especially the presence of high valence rare-earth elements enhancing the catalytic activity. As a result, TM-RE HEO exhibits the best rate capability as well as long-term cycling stability (Figure 3e). Hereby, the results reflect the advantages of a new class of material, HEO to alleviate the shuttling issues of polysulfides and hold great potential as an alternative to carbon host for high-performance sulfur cathode in LSBs. However, the influence of rare earth and transition metal oxides is not well understood yet. In-situ XPS analysis for bonding formation, redox reaction dynamics of the metal oxides are essential to gain new insights into the polysulfide adsorption phenomena.

Conclusions

In summary, this study proposes a novel transition metal and rare-earth elements based high entropy oxide $Co_{0.08}Mn_{0.08}Ni_{0.08}Mg_{0.08}Fe_{1.96}Nd_{0.01}Gd_{0.01}Sm_{0.01}Pr_{0.01}O$ (TM-RE HEO) as an efficient interlayer material to eliminate the polysulfide shuttling issue in LSBs for enhanced cycling performance. It was found that TM-RE HEO outperforms transition metal-based high entropy oxide (TM-HEO) and transition metal rare-earth oxide carbon nanotube composite (TM-REO CNT) as interlayers, attributable to the synergistic function of the elements in a high configurational entropy stabilized structure, boosting the chemical entrapment of polysulfides and catalyzing the redox reaction kinetics. This finding extends the viability of designing and synthesizing new high entropy materials for effective immobilization of polysulfide by tuning the materials composition for high-performance LSBs technology. With an understanding of the detailed adsorption and redox mechanisms, the HEO interlayer can be designed more rationally.

Experimental Section

Materials synthesis: All chemicals were procured from commercial sources (Alfa Aesar/Sigma Aldrich, purity $\geq 98\%$). 1 mM of Co-$(NO_3)_3.6H_2O$, 1 mM of $Mn(NO_3)_2,6H_2O$, 1 mM of $Ni(NO_3)_2,6H_2O$, 1 mM of $Mg(NO_3)_2,6H_2O$, 0.04 mM of $Nd(NO_3)_3,6H_2O$, 0.04 mM of $Gd-(NO_3)_3,6H_2O$, 0.04 mM of $Sm(NO_3)_3,6H_2O$, 0.04 mM of $Pr(NO_3)_3,6H_2O$ and 7.867 mM of $Fe(NO_3)_3,9H_2O$ were dissolved in 90 ml DI water. The homogenous salt solution is transferred to ammonia solution $(NH_3.H_2O)$ dropwise under continuous stirring. Precipitation is obtained after drying in oven at 130 °C overnight, and then it is subjected to calcination at 1000 °C with a dwell time of 2 h. Finally, the product was ground into fine powder. $(CoMnMgNiFe)_3 O_4$ (TM-HEO) was also prepared using the same process. TM-REO CNT was grown through the catalytic decomposition of acetylene gas over as-synthesized TM-RE HEO. The temperature of the furnace was raised to 700 °C at a ramp rate of 10 °C min^{-1} under the argon atmosphere. The hydrogen gas was allowed at 500–700 °C at a flow rate of 0.05 L min^{-1}. Acetylene (flow rate of 0.04 L min^{-1}) was allowed at 700 °C for 30 mins, which led to the growth of carbon nanotubes.

Materials Characterization: Crystalline structure was determined using PXRD (Bruker D_8 Discover) equipped with a Cu-jet X-Ray source (Cu-K_α Radiation, 1.5418 Å). Morphology was examined using SEM (Apreo-S, Thermo-scientific). Drift-corrected elemental mapping was obtained using energy-dispersive X-ray spectroscopy. TEM measurement (HRTEM, SAED) was performed on the powder sample dissolved in ethanol dispersed onto a copper grid and loaded in HR-TEM (JEOL, JEM-2100F, Japan). ULVAC-PHI inc. (Model: PHI5000) K alpha+ spectrometer was used to acquire the XPS spectra. Monochromatic Al K_α radiation was used as X-ray excitation (1486.6 eV) with a pass energy at the electron analyzer of 30 eV (for detailed scan) and 90 eV (for survey scans) to obtain high-resolution spectra. The C 1s peak of carbon at 284.8 eV was used for binding energy calibration. Elemental concentration was determined using ICP-OES. The sample was dissolved in 10 ml HNO_3 and diluted with deionized water up to 50 ml solution, analyzed by performing a double determination using a Perkin Elmer Optima 5300 DV instrument. Chemical composition was analyzed using ICP-MS (NexION 300X).FT-IR spectra are collected from Agilent Technologies Carry 360 FTIR.UV-vis spectroscopy was

performed in a Cary 100 UV-Vis spectrophotometer. EPR studies were carried out in JES-FA200 Electron Spin Resonance Spectrometer.

Electrochemical characterization: Cathode preparation: To prepare the Sulfur cathode, the slurry was prepared by mixing 70 wt.% sulfur as active materials,15 wt.% of PVDF as binder, and 15 wt.% carbon black as conducting additive in NMP solvent and coated on aluminium foil using doctor blade technique followed by drying in a vacuum oven at 80 °C for 10 h. The electrodes were cut into 12 mm disks for further use.

Interlayer preparation: The interlayer was prepared by sonicating 3 mg of HEO in 200 μL of ethanol and 5 μL of Nafion ionomer. The appropriate amount of ink was drop-cast on to a carbon-cloth (15 mm in diameter) followed by drying at 60 °C. The mass loading of sulfur was maintained at 1.5 mg cm^{-2}.

Cell assembly: The electrolyte was prepared using 1 M lithium bis (tri-fluoromethanesulfonyl) imide (LiTFSI) and 0.2 M LiNO$_3$ in a mixture solvent of 1,3-dioxolane(DOL) and 1,2-dimethoxyethane (DME) (1:1 v/v). CR2032 coin cell was assembled with the sulfur cathode, HEO (TM-RE HEO, TM-HEO) as interlayer, lithium metal anode, and GF/C as a separator in an argon-filled glove box (H$_2$O <0.1 ppm and O$_2$ <0.1 ppm). Galvanostatic charge/discharge tests were performed in the potential window of 1.8 V to 2.8 V (vs. Li/Li$^+$) in a Biologic SP300 instrument. Cyclic voltammetry data were collected at different scan rates, and electrochemical impedance spectra (EIS) were examined in the frequency range of 10 mHz to 10 kHz with an amplitude of 5 mV.

Supporting Information

Supporting information is available online or from the author.

Conflict of Interests

The authors declare no conflict of interest.

Data Availability Statement

Research data are not shared.

Keywords: high cycling stability · high entropy oxides · lithium polysulfide entrapment · lithium-sulfur batteries · reaction kinetics

[1] P. G. Bruce, S. A. Freunberger, L. J. Hardwick, J. M. Tarascon, *Nat. Mater.* **2012**, *11*, 19.
[2] X. P. Gao, H. X. Yang, *Energy Environ. Sci.* **2010**, *3*, 174.
[3] Y. T. Liu, S. Liu, G. R. Li, X. P. Gao, *Adv. Mater.* **2021**, *33*, 1.
[4] L. Peng, Z. Wei, C. Wan, J. Li, Z. Chen, D. Zhu, D. Baumann, H. Liu, C. S. Allen, X. Xu, A. I. Kirkland, I. Shakir, Z. Almutairi, S. Tolbert, B. Dunn, Y. Huang, P. Sautet, X. Duan, *Nat. Catal.* **2020**, *3*, 762.
[5] Q. Pang, X. Liang, C. Y. Kwok, L. F. Nazar, *Nat. Energy* **2016**, *1*, 1.
[6] J. Lei, T. Liu, J. Chen, M. Zheng, Q. Zhang, B. Mao, Q. Dong, *Chem* **2020**, *6*, 2533.
[7] H. J. Peng, J. Q. Huang, X. B. Cheng, Q. Zhang, *Adv. Energy Mater.* **2017**, *7*, 1.
[8] B. Zhang, J. Wu, J. Gu, S. Li, T. Yan, X. P. Gao, *ACS Energy Lett.* **2021**, *6*, 537.
[9] P. Chen, G. R. Li, T. T. Li, X. P. Gao, *Adv. Sci.* **2019**, *6*, 1.
[10] S. Li, Z. Fan, *Energy Storage Mater.* **2021**, *34*, 107.
[11] Y. Liang, N. Deng, J. Ju, X. Zhou, J. Yan, C. Zhong, W. Kang, B. Cheng, *Electrochim. Acta* **2018**, *281*, 257.
[12] R. Carter, B. Davis, L. Oakes, M. R. Maschmann, C. L. Pint, *Nanoscale* **2017**, *9*, 15018.
[13] J. Guo, Y. Xu, C. Wang, *Nano Lett.* **2011**, *11*, 4288.
[14] L. Borchardt, M. Oschatz, S. Kaskel, *Chem. Eur. J.* **2016**, *22*, 7324.
[15] D. Liu, C. Zhang, G. Zhou, W. Lv, G. Ling, L. Zhi, Q. H. Yang, *Adv. Sci.* **2018**, *5*.
[16] Y. Song, W. Cai, L. Kong, J. Cai, Q. Zhang, J. Sun, *Adv. Energy Mater.* **2020**, *10*, 1.
[17] H. Yuan, H. J. Peng, B. Q. Li, J. Xie, L. Kong, M. Zhao, X. Chen, J. Q. Huang, Q. Zhang, *Adv. Energy Mater.* **2019**, *9*, 1.
[18] M. Zhao, H. Peng, B. Li, X. Chen, J. Xie, X. Liu, Q. Zhang, J. Huang, *Angew. Chem.* **2020**, *132*, 9096.
[19] Z. Zhang, A. H. Shao, D. G. Xiong, J. Yu, N. Koratkar, Z. Y. Yang, *ACS Appl. Mater. Interfaces* **2020**, *12*, 19572.
[20] R. Razaq, D. Sun, Y. Xin, Q. Li, T. Huang, L. Zheng, Z. Zhang, Y. Huang, *Nanotechnology* **2018**, *29*.
[21] L. Fan, M. Li, X. Li, W. Xiao, Z. Chen, J. Lu, *Joule* **2019**, *3*, 361.
[22] A. Sarkar, L. Velasco, D. Wang, Q. Wang, G. Talasila, L. de Biasi, C. Kübel, T. Brezesinski, S. S. Bhattacharya, H. Hahn, B. Breitung, *Nat. Commun.* **2018**, *9*, 3400.
[23] Y. Chen, H. Fu, Y. Huang, L. Huang, X. Zheng, Y. Dai, Y. Huang, W. Luo, *ACS Mater. Lett.* **2021**, *3*, 160.
[24] G. Liang, J. Wu, X. Qin, M. Liu, Q. Li, Y. B. He, J. K. Kim, B. Li, F. Kang, *ACS Appl. Mater. Interfaces* **2016**, *8*, 23105.
[25] L. Kong, X. Chen, B. Q. Li, H. J. Peng, J. Q. Huang, J. Xie, Q. Zhang, *Adv. Mater.* **2018**, *30*, 1.
[26] X. Liang, C. Y. Kwok, F. Lodi-Marzano, Q. Pang, M. Cuisinier, H. Huang, C. J. Hart, D. Houtarde, K. Kaup, H. Sommer, T. Brezesinski, J. Janek, L. F. Nazar, *Adv. Energy Mater.* **2016**, *6*, 1.
[27] Q. Fan, W. Liu, Z. Weng, Y. Sun, H. Wang, *J. Am. Chem. Soc.* **2015**, *137*, 12946.
[28] T. Wang, H. Chen, Z. Yang, J. Liang, S. Dai, *J. Am. Chem. Soc.* **2020**, *142*, 4550.
[29] Q. Wang, A. Sarkar, D. Wang, L. Velasco, R. Azmi, S. S. Bhattacharya, T. Bergfeldt, A. Düvel, P. Heitjans, T. Brezesinski, H. Hahn, B. Breitung, *Energy Environ. Sci.* **2019**, *12*, 2433.
[30] Y. Zheng, Y. Yi, M. Fan, H. Liu, X. Li, R. Zhang, M. Li, Z. A. Qiao, *Energy Storage Mater.* **2019**, *23*, 678.
[31] L. Tian, Z. Zhang, S. Liu, G. Li, X. Gao, *Energy Environ. Mater.* **2022**, *5*, 645.
[32] W. Hou, P. Feng, X. Guo, Z. Wang, Z. Bai, Y. Bai, G. Wang, K. Sun, *Adv. Mater.* **2022**, *34*, 1.
[33] W. Qu, Z. Lu, C. Geng, L. Wang, Y. Guo, Y. Zhang, W. Wang, W. Lv, Q. H. Yang, *Adv. Energy Mater.* **2022**, *12*, 1.
[34] T. X. Nguyen, J. Patra, J. K. Chang, J. M. Ting, *J. Mater. Chem. A* **2020**, *8*, 18963.
[35] Z. Yan, J. Gao, Y. Li, M. Zhang, M. Guo, *RSC Adv.* **2015**, *5*, 92778.
[36] J. P. Baltrus, M. J. Keller, *Surf. Sci. Spectra* **2019**, *26*, 014001.
[37] M. A. Rahman, R. Radhakrishnan, R. Gopalakrishnan, *J. Alloys Compd.* **2018**, *742*, 421.
[38] D. N. Huh, J. P. Bruce, S. Ganesh Balasubramani, S. R. Ciccone, F. Furche, J. C. Hemminger, W. J. Evans, *J. Am. Chem. Soc.* **2021**, *143*, 16610.
[39] D. Narsimulu, B. N. Rao, G. Nagaraju, J. S. Yu, N. Satyanarayana, *J. Solid State Electrochem.* **2020**, *24*, 225.
[40] X. Pei, R. Wang, *Aerosol Air Qual. Res.* **2019**, *19*, 2888.
[41] Y. Wang, F. Lai, Q. Wang, Q. Long, C. Wang, W. Zhang, Q. Chang, *J. Alloys Compd.* **2022**, *891*, 161932.

[42] Z. Sun, J. Zhang, L. Yin, G. Hu, R. Fang, H. M. Cheng, F. Li, *Nat. Commun.* **2017**, *8*, 14627.

[43] H. Al Salem, G. Babu, C. V. Rao, L. M. R. Arava, *J. Am. Chem. Soc.* **2015**, *137*, 11542.

[44] K. Huang, K. Bi, C. Liang, S. Lin, R. Zhang, W. J. Wang, H. L. Tang, M. Lei, *Sci. Rep.* **2015**, *5*, 1.

[45] R. Elazari, G. Salitra, A. Garsuch, A. Panchenko, D. Aurbach, *Adv. Mater.* **2011**, *23*, 5641.

[46] X. Zhu, W. Zhao, Y. Song, Q. Li, F. Ding, J. Sun, L. Zhang, Z. Liu, *Adv. Energy Mater.* **2018**, *8*, 1.

[47] L. Wang, Z. Y. Wang, J. F. Wu, G. R. Li, S. Liu, X. P. Gao, *Nano Energy* **2020**, *77*, 105173.

[48] Z. Deng, Z. Zhang, Y. Lai, J. Liu, J. Li, Y. Liu, *J. Electrochem. Soc.* **2013**, *160*, A553.

[49] L. Wang, Y. H. Song, B. H. Zhang, Y. T. Liu, Z. Y. Wang, G. R. Li, S. Liu, X. P. Gao, *ACS Appl. Mater. Interfaces* **2020**, *12*, 5909.

[50] B. P. Vinayan, Z. Zhao-Karger, T. Diemant, V. S. K. Chakravadhanula, N. I. Schwarzburger, M. A. Cambaz, R. J. Behm, C. Kübel, M. Fichtner, *Nanoscale* **2016**, *8*, 3296.

[51] T. X. Nguyen, J. Patra, J. K. Chang, J. M. Ting, *J. Mater. Chem. A* **2020**, *8*, 18963.

[52] L. Kong, X. Chen, B. Q. Li, H. J. Peng, J. Q. Huang, J. Xie, Q. Zhang, *Adv. Mater.* **2018**, *30*, 1.

[53] K. P. C. Yao, D. G. Kwabi, R. A. Quinlan, A. N. Mansour, A. Grimaud, Y.-L. Lee, Y.-C. Lu, Y. Shao-Horn, *J. Electrochem. Soc.* **2013**, *160*, A824.

[54] R. Rangel, P. Bartolo-Pérez, E. Martínez, X. A. Trejo-Cruz, G. Díaz, D. H. Galván, *Catal. Sci. Technol.* **2012**, *2*, 847.

[55] H. Sun, G. Chen, Y. Zhu, B. Liu, W. Zhou, Z. Shao, *Chem. Eur. J.* **2017**, *23*, 5722.

[56] Q. Fan, W. Liu, Z. Weng, Y. Sun, H. Wang, *J. Am. Chem. Soc.* **2015**, *137*, 12946.

[57] L. Tian, Z. Zhang, S. Liu, G. Li, X. Gao, *Energy Environ. Mater.* **2022**, *5*, 645.

[58] W. Hou, P. Feng, X. Guo, Z. Wang, Z. Bai, Y. Bai, G. Wang, K. Sun, *Adv. Mater.* **2022**, *34*, 1.

[59] K. Zou, X. Chen, W. Jing, X. Dai, P. Wang, Y. Liu, R. Qiao, M. Shi, Y. Chen, J. Sun, Y. Liu, *Energy Storage Mater.* **2022**, *48*, 133.

[60] S. Xin, T. Liu, J. Li, H. Cui, Y. Liu, K. Liu, Y. Yang, M. Wang, *Small* **2023**, 2207924.

[61] X. Liang, C. Hart, Q. Pang, A. Garsuch, T. Weiss, L. F. Nazar, *Nat. Commun.* **2015**, *6*, 5682.

[62] S. Gope, A. J. Bhattacharyya, *ACS Appl. Energ. Mater.* **2018**, *1*, 2942.

[63] H. Kang, J. Shin, T. H. Kim, Y. Lee, D. Lee, J. Lee, G. Kim, E. A. Cho, *ACS Sustainable Chem. Eng.* **2023**, *11*, 1344.